

OPEN ACCESS

# Impact of Polymer Interlayers on All-Solid-State Battery Performance Using a Physicochemical Modeling Approach

To cite this article: M. Scheller *et al* 2024 *J. Electrochem. Soc.* **171** 020509

View the [article online](#) for updates and enhancements.

## You may also like

- [Review—Electrospun Inorganic Solid-State Electrolyte Fibers for Battery Applications](#)  
Jaswinder Sharma, Georgios Polizos, Charl J. Jafta et al.
- [Investigation of the Ionic Conduction Mechanism of Polyether/Li<sub>7</sub>La<sub>3</sub>Zr<sub>2</sub>O<sub>12</sub> Composite Solid Electrolytes by Electrochemical Impedance Spectroscopy](#)  
Masaki Kato, Koji Hiraoka and Shiro Seki
- [Stable Lithium Plating in “Lithium Metal-Free” Solid-State Batteries Enabled by Seeded Lithium Nucleation](#)  
Catherine Haslam and Jeff Sakamoto



## Your Lab in a Box!

The PAT-Tester-i-16: All you need for Battery Material Testing.

- ✓ All-in-One Solution with integrated Temperature Chamber!
- ✓ Cableless Connection for Battery Test Cells!
- ✓ Fully featured Multichannel Potentiostat / Galvanostat / EIS!

[www.el-cell.com](http://www.el-cell.com) +49 40 79012-734 [sales@el-cell.com](mailto:sales@el-cell.com)

**EL-CELL**<sup>®</sup>  
electrochemical test equipment





# Impact of Polymer Interlayers on All-Solid-State Battery Performance Using a Physicochemical Modeling Approach

M. Scheller,<sup>1,2,z</sup> A. Durdal,<sup>1</sup> A. Frank,<sup>1</sup> J. Kriegler,<sup>3</sup> and A. Jossen<sup>1</sup>

<sup>1</sup>Technical University of Munich (TUM), TUM School of Engineering and Design, Department of Energy and Process Engineering, Chair of Electrical Energy Storage Technology, Arcisstr. 21, 80333 Munich, Germany

<sup>2</sup>TUMint Energy Research GmbH, Lichtenbergstr. 4, 85748 Garching b. München, Germany

<sup>3</sup>Technical University of Munich (TUM), TUM School of Engineering and Design, Department of Mechanical Engineering, Institute for Machine Tools and Industrial Management, Boltzmannstr. 15, 85748 Garching b. München, Germany

Recent studies presented the advantages of incorporating solid-polymer-electrolyte (SPE) interlayers in all-solid-state batteries (ASSB). Still, drawbacks regarding the cell performance are expected due to additional polymer-related overpotentials. The pseudo-two-dimensional (p2D) physicochemical model is extended to account for Li-ion transport in the SPE interlayer and in the ceramic LLZO solid electrolyte (SE), as well as for the charge transfer at the SPE|LLZO interface using Butler-Volmer-like kinetics. The overpotential analysis for a reference parameterization disclosed a dominant overpotential contribution from the SPE|LLZO charge transfer and a facilitation with increasing discharge C-rate. Variance-based global sensitivity analyses demonstrate that as the exchange current density between SPE and LLZO increases, polarization losses exhibit an exponential-like reduction. Additionally, the radius of the active material (AM) particles within the composite cathode exerts a significant and dominant influence on cell performance. With an optimization of the SPE|LLZO exchange current density, the accessible capacity could be increased compared to the reference parameterization from 41% to 61% for a 2C discharge.

© 2024 The Author(s). Published on behalf of The Electrochemical Society by IOP Publishing Limited. This is an open access article distributed under the terms of the Creative Commons Attribution 4.0 License (CC BY, <http://creativecommons.org/licenses/by/4.0/>), which permits unrestricted reuse of the work in any medium, provided the original work is properly cited. [DOI: 10.1149/1945-7111/ad1e3e]



Manuscript submitted September 26, 2023; revised manuscript received December 2, 2023. Published February 8, 2024.

## List of Symbols

### Physical Constants

$\mathcal{F}$  Faraday's constant, 96 487 C mol<sup>-1</sup>  
 $\mathcal{R}$  universal gas constant, 8.341 J mol<sup>-1</sup> K<sup>-1</sup>

### Modeling

$i$  current density A m<sup>-2</sup>  
 $i_0$  charge transfer exchange current density, A m<sup>-2</sup>  
 $\alpha$  transfer coefficient, 0.5, *unitless*  
 $\Delta\phi$  electric potential difference, V  
 $\epsilon$  material volume fraction, vol%  
 $\kappa$  ionic conductivity, S m<sup>-1</sup>  
 $\Omega$  model domains, Fig. 1  
 $c_{Li}$  Li-cation concentration, mol m<sup>-3</sup>  
 $D$  salt diffusion coefficient, m<sup>2</sup> s<sup>-1</sup>  
 $E_{loss}$  overpotential related energy losses, Wh m<sup>-2</sup>  
 $E_{th}$  theoretical areal energy, Wh m<sup>-2</sup>  
 $Q_{th}$  theoretical areal capacity, Ah m<sup>-2</sup>  
 $r_{pos}$  active material particle radius,  $\mu$ m  
 $T$  temperature, 353 K  
 $t$  component/domain thickness,  $\mu$ m  
 $t_+$  Li-cation transference number, *unitless*  
 $T_{EoD}$  time of end-of-discharge, s  
 $TDF$  thermodynamic factor, *unitless*  
 $U_{cell}$  simulated cell voltage, V  
 $U_{eq}$  cathode active material equilibrium potential, V

### Sensitivity Analysis

A+ sensitivity study type, Anode "side" improvement, *unitless*  
 A- sensitivity study type, Anode "side" deterioration, *unitless*  
 C+ sensitivity study type, Cathode "side" improvement, *unitless*  
 C- sensitivity study type, Cathode "side" deterioration, *unitless*

## Subscripts

AM active material  
 ct charge transfer  
 if related to SPE|LLZO interface  
 LLZO related to ceramic LLZO separator domain  
 POS related to cathode domain  
 SE solid electrolyte  
 SPE related to solid-polymer electrolyte domain

## Motivation and Literature

Over the last years, Li-ion batteries became the energy storage system of choice for nearly all mobile applications and electric vehicles.<sup>1</sup> Current state-of-the-art battery cells in electric vehicles achieve a specific energy around 260 Wh kg<sup>-1</sup> and an energy density of 700 Wh l<sup>-1</sup>, leading to a typical driving range from 300 km to 500 km.<sup>2,3</sup> Fast-charging of electric vehicles to 80% state-of-charge (SoC) currently takes approximately 30 min. To eliminate customers' range-anxiety, an improvement toward higher energy density and better fast-charging performance is still needed. Therefore, battery research strengthens the focus toward next-generation batteries. Advances in the ionic conductivity of inherently safe solid electrolytes (SE) combined with high-energy lithium metal anodes make the solid-state battery (ASSB) one of the most promising representatives of the next generation of batteries.<sup>2,4</sup> Besides the expected performance improvement from a single component perspective, several challenges must be solved for building a high-performance, inherently safe, low-cost, and large-format batteries that are industrially fabricable.

On behalf of cell performance, one main challenge is achieving electrochemical and mechanical stable interfaces between solid components during cycling while maintaining a low cell resistance.<sup>5</sup> Due to the high ionic conductivity of up to 25 mS cm<sup>-1</sup> and a lithium transference number close to unity, inorganic solid electrolytes (ISE) are the first choice for high-performance ASSBs.<sup>4</sup> The electrochemical instability of most ISEs triggers material decomposition, resulting in interphase formation at anode and cathode interfaces.<sup>6</sup> In addition, volume changes of anode and cathode active materials (AM) lead to contact loss and AM particle cracking, deteriorating the ionic transport properties.<sup>7-9</sup> High external pressures in the

<sup>z</sup>E-mail: [maximilian.scheller@tum.de](mailto:maximilian.scheller@tum.de)

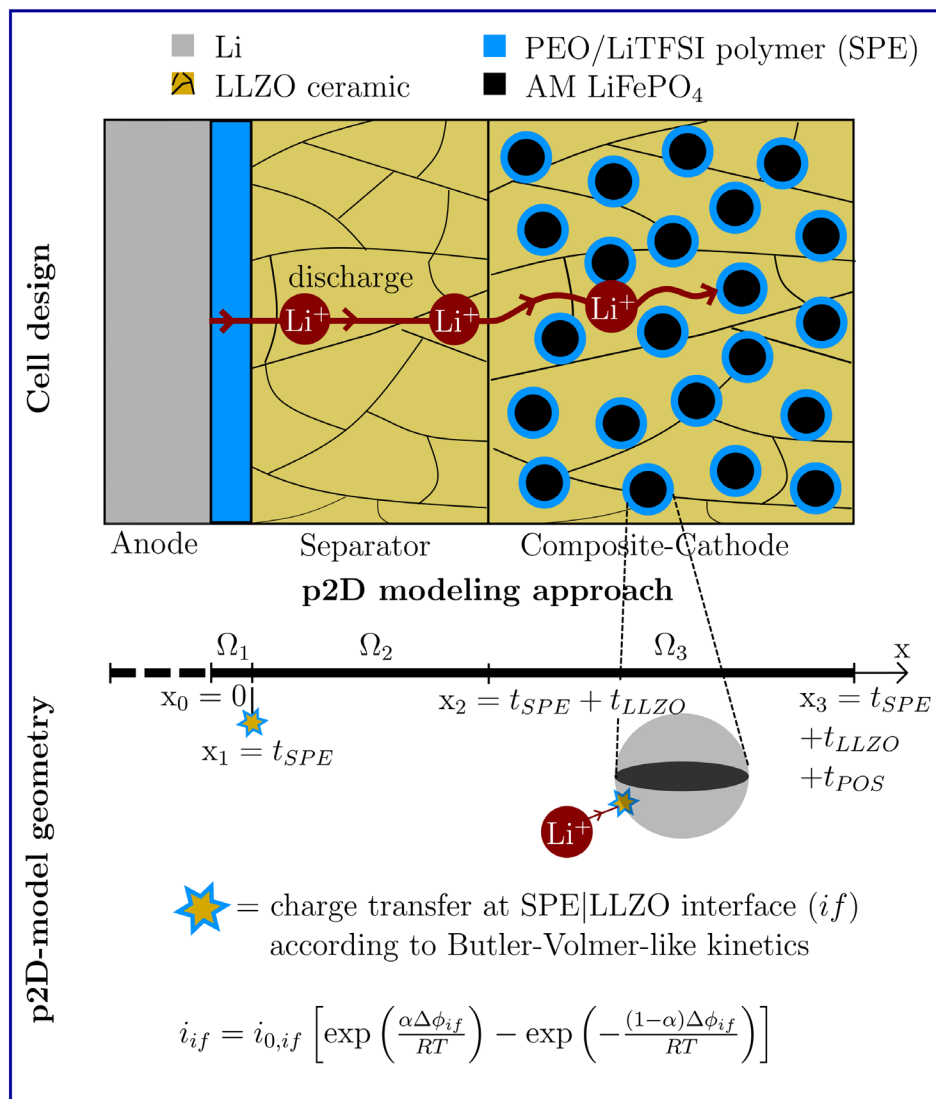


**Figure 1.** Schematic of cell design consisting of a Li-metal anode, an LLZO ceramic SE separator (domain:  $\Omega_2$ ) and an LLZO/LFP composite cathode (domain:  $\Omega_3$ ). As highlighted in blue, an interlayer of PEO/LiTFSI SPE (domain:  $\Omega_1$ ) is incorporated on the Li-metal anode, and as a coating on LFP particles. The Li-ion transport pathway during discharge is highlighted in red. The Li ions must cross the SPE|LLZO interface two times. In the p2D-model geometry, the additional overpotential at the SPE|LLZO interface at  $x = x_1$  and at the AM particle surface  $r = r_{pos}$  is modeled with a Butler-Volmer-like charge transfer kinetic.

megapascal range are implemented on lab-scale as they improve cycling performance and reduce contact loss, but they lead to additional challenges for up-scaling and production.<sup>10–12</sup>

An alternative way to maintain stability and intimate contact at anode and cathode interfaces is the usage of solid-polymer electrolyte (SPE) coatings or interlayers. Polymer coatings on cathode AM could avoid electrochemical instabilities between the ISE and AM, due to the wide electrochemical stability window of most polymers.<sup>13,14</sup> Recently, Deng et al.<sup>15</sup> used a 5 nm poly(3,4-ethylenedioxythiophene) (PEDOT) Polymer coating to prevent Li<sub>10</sub>GeP<sub>2</sub>S<sub>12</sub> (LGPS) ISE degradation. In doing so, the capacity retention at 1C increased tenfold compared to the usage of bare LGPS.<sup>15</sup> Furthermore, stabilizing interfaces in the cathode using polymer coatings is also known for high-voltage cathode AM in contact with liquid electrolytes. An overview of cycling data for different types of electrolytes in contact with polymer-coated AM is provided by Sen et al.<sup>14</sup> Furthermore, volume changes of the AM during operation can be compensated by the flexible nature of polymers.<sup>14</sup> As a result, crack formation, which is observed for AM in contact with rigid ISEs, could be reduced.<sup>7</sup> Additionally, a large contact area between AM and SPE is expected, which leads to a low interfacial resistance.<sup>14</sup>

Polymer interlayers in contact with the Li-metal anode serve the same purposes compared to AM coatings in composite cathodes. They should prevent continuous decomposition reactions between Li-metal and the ISE, due to their large electrochemical stability window. Furthermore, due to the mechanical flexibility of the SPE interlayer, better physical contact with the Li-metal anode is expected in comparison to direct contact with the ISE. This could pave the way for homogeneous plating and stripping characteristics and reduced dendrite formation.<sup>14,16–18</sup>

Besides the presented advantages using polymer coatings or interlayers in combination with ISE in ASSBs, possible drawbacks have to be mentioned. The major disadvantage of SPE including Li-ion conductive salts are the poor ionic transport properties at room temperature, with typical ionic conductivities of around  $10^{-5}$  S cm<sup>-1</sup>, a diffusivity of  $10^{-9}$  cm<sup>2</sup> s<sup>-1</sup>, and a rather low transference number of  $<0.3$ .<sup>19–21</sup> Depending on polymer layer thickness, current density, and conductive salt content, polarization and performance limitations arise.<sup>20</sup> To prevent such problems, batteries containing SPEs are typically cycled and characterized at elevated temperatures between 60 °C and 90 °C.<sup>19–21</sup> Furthermore, the introduction of polymer interlayers implements an additional

interface between the SPE and the ISE, influencing ionic transport between the electrodes. Several studies analyzed the charge transfer resistance between SPE and different ISEs via impedance spectroscopy. As result, the charge transfer resistance is strongly dependent on the conductive salt content in the SPE, and a significant voltage drop over the interface has to be expected.<sup>22–24</sup>

The presented advantages of SPE interlayers lead to the question of whether hybrid cell designs incorporating SPE and ISEs is of practical relevance in relation to cell performance, considering the comparably poor ionic transport properties of SPE and additional interfaces. This study aims for a consideration of additional SPE layers and related interface charge transfer in an ASSB full-cell model. With this approach, experimental results from the literature on the kinetics at SPE|ISE interfaces are analyzed in relation to their impact on ASSB full-cell performance for the first time. First, an analysis of the significant physicochemical effects causing polarization, leading to performance limitations due to polymer interlayers in ASSBs was performed. To this end, the classical p2D Doyle-Fuller-Newman (DFN) model, typically used for liquid-electrolyte Li-ion batteries, was adapted to account for ionic transport in the ISE and additional charge transfer at the SPE|ISE interface. In the modeling section, significant literature on the adaptations of the DFN model to address ionic transport in ISE and SPE, as well as charge transfer at the SPE|ISE interface will be discussed. Since the model allows access to spatially resolved internal states like concentrations and potentials, the total overpotential can be separated based on the underlying physicochemical effects. In doing so, the overpotential caused from polymer interlayer related effects can be analyzed. Second, a variance-based global sensitivity analysis is performed to analyze the sensitivity of overpotentials on the polymer material properties and related geometric input parameters. From the sensitivity analysis, important input parameters are identified and analyzed toward their potential for improvement of cell performance. Finally, the model-based comparison of rate capability between different parameterizations with and without polymer interlayers disclose the practical relevance of ASSBs containing polymer interlayers.

## Methodology

**Physicochemical modeling.**—The modeled cell design is depicted in Fig. 1 and consists of a Li-metal anode, a SPE interlayer ( $\Omega_1$ ) in contact with the Li-metal anode, an ISE separator ( $\Omega_2$ ), and the composite cathode ( $\Omega_3$ ) with SPE-coated LFP-AM and LLZO SE. As a basis for the electrochemical model, the p2D modeling approach, introduced by Doyle, Fuller and Newman, was chosen.<sup>25–27</sup> Besides the classical use case for modeling liquid electrolyte cells, this model approach was already used for ASSBs with binary salt SPEs or inorganic single-ion conducting SEs.<sup>28,29</sup> In comparison to cell designs containing only one type of electrolyte, an additional charge transfer process at the SPE|LLZO interface has to be considered for this cell setup. Two different approaches are present in literature to consider the overpotential due to charge transfer at the SPE/ceramic SE interface. First, in the theoretical model framework of Kim et al.,<sup>30</sup> the junction potential theory was used to calculate the potential drop between a PEO-based SPE and an LLZO SE in hybrid solid-electrolytes.<sup>27</sup> The theory considers the difference in Li-ion concentrations in the adjacent materials to calculate the potential drop at the interface. This approach could be valuable for purely model-based studies, but needs further experimental validation for different combinations of SPE in contact with ISE. Therefore, we recommend further research in that field.

Second, Schleutker et al.<sup>31</sup> and Brogioli et al.<sup>32</sup> derived an adopted Butler-Volmer-like (BV) kinetic for the charge transfer at a liquid electrolyte|LLZTO SE interface and a SPE|LLZO interface, respectively. The difference in chemical potentials between liquid and solid binary salt-type electrolytes and single-ion conducting ceramic SE results in an electric potential difference across the interface. In assuming a thermally activated charge transfer process for the mass transport over the interface, the relation between current and overpotential can be described with a BV-like kinetic. Furthermore, it was

experimentally determined that the dependency of the charge transfer resistance on the salt concentration follows a power law. At higher binary salt concentrations, a deviation from the power law was observed due the presence of interphases or space charge layers.<sup>31,32</sup>

Analogous to this, Isaac et al.<sup>33</sup> derived and validated experimentally that the charge transfer resistance at the phase boundary between a PEO/LiTFSI-0.6M SPE and a glass ceramic SE (Ohara corp.) decreases with increasing salt concentration, following a power law. A purely BV-like kinetic over a large range of binary salt concentrations was obtained in their measurements. By this, a constant activity coefficient of one could be assumed in the SPE and no additional interphase formation at high salt concentrations has occurred. Isaac et al. summarized that several research groups discovered deviations of the measured charge transfer resistance  $R_{ct,if}$  from a purely BV-like kinetic at high salt concentrations, which are due to the formation of space-charge layers or interphases.<sup>22,32,34</sup>

This study captures the charge transfer at the SPE|LLZO interface using a purely BV-like kinetic, assuming no interphase formation or a considerable extension of the space-charge layer. Therefore, the relation between current density  $i_{if}$  and the difference in electric potential at the SPE|LLZO interface  $\Delta\phi_{if}$  can be described according to Eq. 1. Additional, a potential boundary condition for  $\Delta\phi_{if}$  is discussed later in Eq. 7. The transfer coefficient  $\alpha_{if}$  describes the symmetry between anodic and cathodic charge transfer. For a consistent allocation, all parameters in relation to the charge transfer at the SPE|LLZO interfaces are marked with the subscript *if* hereafter.

$$i_{if} = i_{0,if} \left[ \exp\left(\frac{\alpha_{if} \Delta\phi_{if}}{\mathcal{RT}}\right) - \exp\left(-\frac{(1 - \alpha_{if}) \Delta\phi_{if}}{\mathcal{RT}}\right) \right] \quad [1]$$

For small currents, the exchange current density  $i_{0,if}$  can be calculated according to

$$i_{0,if} = \frac{\mathcal{RT}}{\mathcal{F}R_{ct,if}} \quad [2]$$

The charge transfer resistance  $R_{ct,if}$  follows a power law with increasing salt concentration in the polymer phase and is proportional to

$$R_{ct,if} \propto c_{Li,SPE}^{-(1-\alpha_{if})} \quad [3]$$

To conserve charge at the SPE|LLZO interface, assuming no side reactions, the current densities in SPE and LLZO SE must be equal at the boundary according to Eq. 4. Analogous to this, the total Li-ion flux in the SPE and LLZO phase must be equal at the boundary to conserve mass according to Eq. 5. Equation 6 clarifies the relation between electrophoretic and diffusive fluxes in the SPE and LLZO phase. Due to immobile anions in the single-ion conducting LLZO electrolyte, the total Li-ion flux is covered by electrophoretic charge transport. The number of proton charge carried by a Li ion is  $z_{Li^+} = 1$  and can therefore be neglected in Eq. 6. The overpotential at the SPE|LLZO interface, calculated from the BV relation, has to be considered in the calculation of the electrolyte potential in the SPE and LLZO phase according to Eq. 7, respectively.

$$i_{SPE} = i_{LLZO} \quad [4]$$

$$J_{Li,SPE} = J_{Li,LLZO} \quad [5]$$

$$-D_{Li,SPE} \frac{\partial c_{Li,SPE}}{\partial x} + \frac{i_{SPE} t_+^{SPE}}{\mathcal{F}} = \frac{i_{LLZO}}{\mathcal{F}} \quad [6]$$

$$\Delta\phi_{if} = \phi_{LLZO} - \phi_{SPE} \quad [7]$$

For numerical solving of the governing equations (see Table A-1) of the adapted p2D model, COMSOL Multiphysics 6.0 was used.

The solver sequence conforms with the software recommendations for the given set of equations according to Table A.1.

**Model assumptions and parameterization.**—To get a consistent set of model parameters, we decided to parameterize the cell model with data from the literature for an elevated temperature at around 80 °C. Furthermore, isotropic properties for the SE and AM phases are assumed. Values for all used parameters regarding the cell properties, ionic and electronic transport, and kinetics are listed in Table I.

As depicted in Fig. 1, the Li-metal anode was modeled as a boundary condition, due to its non-limiting electronic conductivity of  $10^7 \text{ S m}^{-1}$ . At  $x = 0$ , the charge transfer between Li-metal and the SPE interlayer was modeled with BV-like kinetics.

To consider ionic transport in the SPE ( $\Omega_1$ ), concentrated solutions theory was applied, capturing Li-ion transport through migration and diffusion. A set of salt concentration dependent transport parameters according to Pesko et al.<sup>19</sup> was chosen for SPE parameterization. For the reference parameterization, the equilibrium salt concentration was chosen to be  $c_{Li,SPE} = 1960 \text{ mol m}^{-3}$ . Additionally, recent studies show that Li-ion transport in SPEs is influenced by polymer motion. Mistry et al.<sup>40</sup> presented a modification of concentrated solution theory to account for polymer motion within the governing model equations. Their results indicated a significant impact of polymer motion on the Li-ion flux through a 500  $\mu\text{m}$  thick PEO/LiTFSI polymer layer, which is sensitive to the initial salt concentration and related transference number  $t_+$ . Since this study is focusing on polymer coatings, the polymer layer thickness is comparably small with a maximum layer thickness of  $t_{SPE} = 10 \mu\text{m}$ . Therefore, simpli-

fied preliminary studies showed only a small change of concentration gradients if polymer motion was considered. Since this change in concentration gradient does not significantly impact charge transport overpotentials, polymer motion was neglected in this study.

Due to the single-ion conducting nature of LLZO SE caused from immobile anions, a transference number of  $t_+ = 1$  can be assumed, leading to pure electrophoretic Li-ion transport in the LLZO SE phases.<sup>41</sup> Therefore, no Li-ion concentration gradients exist in the LLZO phases.

The porous electrode approach in the cathode ( $\Omega_3$ ) treated the microstructure of the composite cathode as a homogenized geometry with uniform spherical LFP-AM particles with radius  $r_{pos}$ , which are in ideal contact with the LLZO SE. Necessary inactive components to achieve sufficient, non-limiting electronic conductivity like carbon-binder and possible voids are considered by assuming an inactive volume of  $\varepsilon_{void} = 10 \text{ vol. \%}$ .

To represent the elongated transport pathways due to the microstructure in a 1D-model, the diffusivity  $D_{SE}$  in the electrolyte domain, as well as the ionic conductivity  $\kappa_{SE}$ , and electronic conductivity  $\sigma_{SE}$  must be corrected via the tortuosity  $\tau$  and porosity  $\epsilon$  of the electrode.<sup>42,43</sup> Polarization due to bulk transport in the SPE coating was neglected, since the thickness of AM coatings is in practice in the single-digit nanometer range.<sup>44,45</sup> Therefore, the SPE coating on the AM particles was not spatially resolved and can be interpreted as a 0D-component, which adds an additional resistance contribution, arising from the SPE/LLZO interface charge transfer. The additional potential drop from the SPE/LLZO charge transfer was calculated via an analytical formulation of the BV equation according to Eq. 8, which can be used as a simplification due to a

**Table I. Reference parameterization of the p2D model with an additional SPE interlayer and AM particle coating, separated for each model domain.**

Parameter	Symbol	Unit	SPE $\Omega_1$	LLZO $\Omega_2$	Cathode $\Omega_3$	Source
<b>Geometry</b>						
Thickness	$t$	$\mu\text{m}$	5	20	120	
Particle radius	$r_{pos}$	$\mu\text{m}$	—	—	1	
Active material fraction	$\varepsilon_{AM}$	vol.%	—	—	50	
SE material fraction	$\varepsilon_{SE}$	vol.%	100	100	40	
Inactive material/void fraction	$\varepsilon_{void}$	vol.%	—	—	10	35
Tortuosity	$\tau$	—	—	—	4	35
<b>Transport<sup>(a)</sup></b>						
Diffusivity SE	$D_{SE}$	$\text{m}^2 \text{ s}^{-1}$	$7.88 \cdot 10^{-12}$	—	—	36
Ionic conductivity SE	$\kappa_{SE}$	$\text{S m}^{-1}$	0.12	0.1	0.1	19, 34
Diffusivity AM	$D_{AM}$	$\text{m}^2 \text{ s}^{-1}$	—	—	$6 \cdot 10^{-16}$	37
Electronic conductivity	$\sigma$	$\text{S m}^{-1}$	—	—	100	non-limiting
Transference number	$t_+$	—	0.086	1	1	19
Thermodynamic factor	$TDF$	—	3.34	1	1	19, 21
<b>Kinetics</b>						
AM exchange current	$i_{0,AM,x}$	$\text{A m}^{-2}$	$220 _{x=x_0}$	—	$0.30 _{r=r_{pos}}$	38 calc. Eq. 2
Interface exchange current	$i_{0,if,x}$	$\text{A m}^{-2}$	$1.07 _{x=x_1}$	—	$1.07 _{r=r_{pos}}$	calc. Eq. 2
Transfer coefficient	$\alpha$	—	—	0.5 <sup>(b)</sup>	—	
<b>Cell</b>						
LFP Equilibrium Potential	$U_{eq}$	V	—	—	—	37
Cell potential start	$U_{cell,init}$	V	—	—	4.13	
Cell potential end	$U_{cell,end}$	V	—	—	2.80	
Areal capacity	$Q_{th}$	$\text{Ah m}^{-2}$	—	—	35.1	calc.
Areal energy	$E_{th}$	$\text{Wh m}^{-2}$	—	—	123.5	calc.
<b>Concentration dependent parameters</b>			<b>Argument/Unit</b>		<b>Function/Unit</b>	
PEO LFP charge transfer resistance $R_{ct,PEO LFP}$			$a = \frac{c_{Li,LFP}}{c_{max,Li,LFP}} / -$		$0.08829 \cdot a^3 - 0.2153 \cdot a^2 + 0.08799 \cdot a + 0.09354 / \Omega \text{ m}^2$ <sup>39</sup>	
PEO LLZO charge transfer resistance $R_{ct,if}$			$c_{Li,SPE} / \text{mol m}^{-3}$		$1.048 \cdot c_{Li,SPE}^{-0.4986} / \Omega \text{ m}^2$ <sup>32</sup>	
SPE transport parameters			see Pesko et al. <sup>19</sup> for analytical expressions			

a) SPE transport parameters are concentration dependent and here evaluated at  $c_{Li,SPE} = 1960 \text{ mol m}^{-3}$ . b) Assuming symmetric charge transfer for all reactions.



transfer coefficient of  $\alpha_{if} = 0.5$ .<sup>46</sup>

$$\Delta\phi_{if,r_{pos}} = \frac{2\mathcal{R}T}{\mathcal{F}} \operatorname{arc\,sinh}\left(\frac{i_{if,r_{pos}}}{2i_{0,if,r_{pos}}}\right) \quad [8]$$

This additional potential drop has to be considered in the governing equations. Therefore, the charge transfer potential boundary condition at the AM particle surface has to fulfill the following equation:

$$\Delta\phi_{ct,PEO|LFP} = \phi_{LFP} - \phi_{LLZO} - U_{eq} - \Delta\phi_{if,r_{pos}} \quad [9]$$

Furthermore, side reactions were neglected in the model, assuming that all components in direct contact are electrochemically stable. This is also why LFP was chosen, as nickel-rich AM is prone to side reactions in contact with a PEO based SPE electrolyte.<sup>47</sup>

**Overpotential analysis.**—To get information on the spatial distribution of overpotentials and their underlying physicochemical effects, spatially resolved information of potential and concentration distributions can be used according to Nyman et al.<sup>48</sup> This framework is used to calculate the shares of polarization regarding the diffusion and ohmic related processes in the SPE, ohmic overpotential in the single-ion conducting LLZO phases, overpotential related to diffusion in the AM, and charge transfer overpotential related to the (de)lithiation processes.<sup>48,49</sup> In addition to the work from Nyman et al., the charge transfer overpotentials at the SPE|LLZO interfaces are considered in this work. The governing equations regarding the calculation of the different overpotential contributions are listed in Table A.II.

**Global sensitivity analysis.**—When it comes to physicochemical modeling of Li-ion batteries, typically, a measurement-based characterization of the cell of interest is conducted to get information about cell geometry, electrical and thermal behavior, as well as morphological and material information.<sup>37,50</sup> The parameterization of transport and kinetic-related parameters is either based on literature values or proprietary material characterizations. If no values are available, fitting presents an alternative method, however, limiting the modeling validity. Currently, the restricted availability

of commercial ASSBs prohibits the acquisition of comprehensive datasets for parameterizing physicochemical battery cell models.

An essential step involves critically assessing the parameters gathered from the literature, given that parameter determination can vary when sourced from different studies, laboratories, and individuals. Therefore, it is crucial to review the range of input parameters provided by the literature. To this end, a global sensitivity analysis was used in this study to capture the sensitivity of the model output with regard to the input parameters. In this scientific use-case, the global sensitivity analysis facilitates a deeper understanding of the system. It can uncover unexpected dependencies, parameter interactions, or non-linear effects that were not previously known. These information are used in this study to reveal potentials for battery performance optimization.<sup>51,52</sup>

Sobol' sensitivity indices can give a quantitative ranking of input parameters regarding their contribution to the variance of the model output, taking into account parameter interactions.<sup>53</sup> The Sobol' method decomposes the total variance of the model output into contributions from individual parameters and parameter interactions. Typically, two different indices are evaluated. The first-order Sobol' index measures the contribution to the total variance from each individual parameter, independently of other parameters. The total-order Sobol' index additionally includes the contribution from input parameter interactions to the total variance of the model output. The evaluation of Sobol' indices was already applied in previous modeling studies on Li-ion batteries with both liquid and solid electrolytes.<sup>29,54</sup>

The conducted process steps to evaluate the variance-based Sobol' indices are illustrated in the process diagram in Fig. 2. Starting with the fully parameterized p2D physicochemical model with multiple-input and multiple-output parameters, a scalar output parameter has to be defined in the next step, which gives valuable information in relation to the research question. In this study, the total losses due to cell overpotentials during discharge can be captured by calculating the power losses at each timestep. The power losses are based on the total overpotential ( $U_{eq} - U_{cell}$ ) and the applied constant current  $i_{app}$ . The time-integral until the end-of-discharge (EoD) then yields the total losses in relation to the electrode area in  $\text{Wh m}^{-2}$ . This parameter is defined as  $E_{loss}$  according to equation Eq. 10 and set as the Quantity-of-Interest

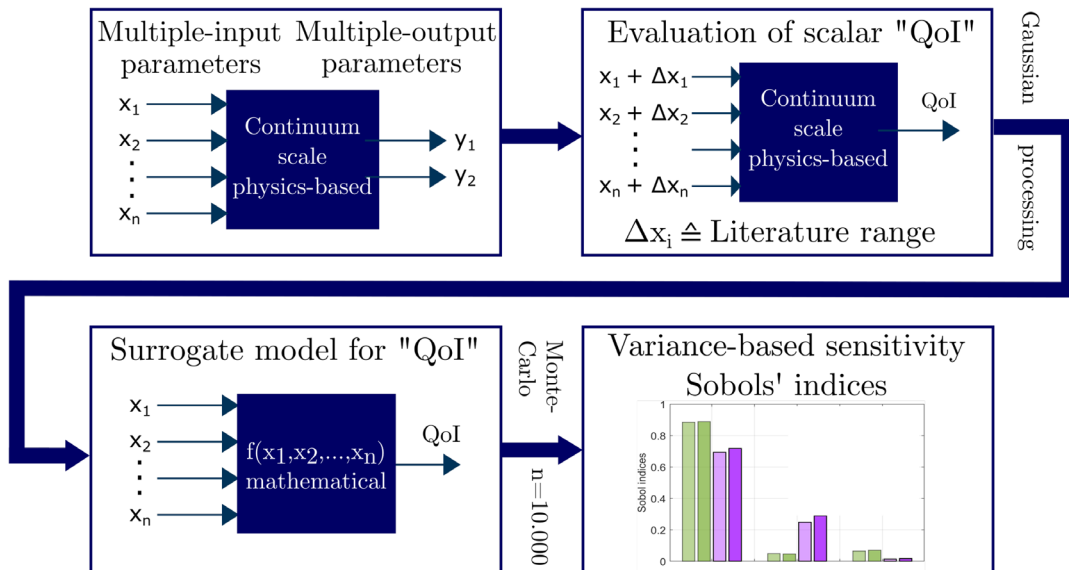


**Figure 2.** Process diagram for variance-based global sensitivity analysis, evaluating Sobol' indices. Starting from the p2D physics-based model with multiple input and output parameters, the uncertainty range of each input parameter was defined based on the known literature values  $\Delta x_i$  and a scalar quantity-of-interest (QoI) was defined. UQlab was used to calculate a mathematical surrogate model for the QoI using gaussian processing. With the low computational effort of the surrogate model, it was possible to perform a Monte-Carlo simulation with 10,000 evaluations in order to calculate the Sobol' indices.<sup>55</sup>

**Table II.** Input parameter variations based on the literature range to study the sensitivity of the defined QoI  $E_{loss}$ . Two groups of parameters were defined to measure the sensitivity of the QoI on SPE-related parameters on “anode” side and “cathode” side, respectively. For each group, two sensitivity studies were conducted in this work, investigating the improvement (Study A+ and C+) and the deterioration (Study A– and C–) of each chosen input parameter based on the reference parameterization.

Parameter	Unit	Reference	Minimum	Maximum	Source	Sensitivity study			
Study type						A+	A–	C+	C–
<b>“Anode” side</b>									
$t_{SPE}$	$\mu\text{m}$	5	1	10		min	max		
$\kappa_{SPE}$	$\text{S m}^{-1}$	0.12	0.07	0.22	19	max	min		
$D_{SPE}$	$\text{m}^{-2} \text{s}^{-1}$	$7.88 \cdot 10^{-12}$	$6.2 \cdot 10^{-12}$	$1 \cdot 10^{-11}$	36	max	min		
$t_{+,SPE}$	–	0.086	0.086	0.9	a)	max	min		
$TDF_{SPE}$	–	3.34	0.6	6	19,21	min	max		
$i_{0,if,x1}$	$\text{A m}^{-2}$	1.07	0.036	32	32,33	max	min		
<b>“Cathode” side</b>									
$r_{pos}$	$\mu\text{m}$	1	0.2	5	58			min	max
$i_{0,AM,r_{pos}}$	$\text{A m}^{-2}$	0.3	0.1	3	24,59,39,60			max	min
$i_{0,if,r_{pos}}$	$\text{A m}^{-2}$	1.07	0.036	32	32,33			max	min

a) development toward single-ion conducting SPE.

(QoI) for the sensitivity analysis. The theoretical energy content of the cell calculates to  $E_{th} = 123.5 \text{ Wh m}^{-2}$  (see Table I).

$$E_{loss} = \int_0^{T_{EoD}} i_{app}(U_{eq} - U_{cell}) dt \Big|_{x=l_{cell}} \quad [10]$$

Besides the definition of the QoI, the input parameters which should be considered in the sensitivity analysis and their underlying range have to be defined. The p2D physicochemical model requires over 30 different input parameters.<sup>56</sup> Therefore, a sensitivity analysis considering all parameters would result in large computational effort. Additionally, the sensitivity to most of the input parameters was already investigated in previous studies.<sup>29,57</sup> Landesfeind et al.<sup>57</sup> investigated the sensitivity of the critical current density and the overpotential of an NMC/graphite liquid electrolyte cell. They concluded that the key factors to improve cell performance are the electrolyte transport properties and the electrodes’ tortuosity and porosity. Thoghiani et al.<sup>29</sup> investigated the sensitivity of the gravimetric energy density of an ASSB cell with a hybrid solid electrolyte in relation to seven different model input parameters. As their goal was to improve performance with an optimized cell design, they identified the thickness of the SE separator, the thickness of the cathode, and the AM content in the cathode as the most relevant parameters regarding the gravimetric energy density.

Since the main goal of this study is to analyze the impact of polymer interlayers on the ASSB cell performance, the following input parameters were analyzed in the sensitivity studies. This includes the SPE layer thickness  $t_{SPE}$ , the ionic conductivity  $\kappa_{SPE}$  and diffusivity  $D_{SPE}$ , the transference number of the SPE phase  $t_{+,SPE}$ , as well as the thermodynamic factor in the SPE  $TDF_{SPE}$ . The ranges of the SPE transport parameters according to Table II were defined based on their equilibrium salt concentrations used in the respective references. Therefore, the variation of SPE transport parameters in dependence of the choice of the equilibrium concentration  $c_{Li,SPE}$  was considered in the sensitivity studies.

Furthermore, the charge transfer kinetics at the SPE|LLZO interface have to be considered. A suitable parameter to realize a variation of interfacial charge transfer is the exchange current density  $i_{0,if}$  and is therefore added to the sensitivity studies. Concerning the SPE coating on the AM in the composite cathode, the particle radius  $r_{pos}$  directly affects the active surface area of the charge transfer and thus, has a direct relation to the charge transfer overpotential at the SPE|LLZO interface. The input parameters for

the sensitivity studies are listed in Table II. The reference value of each parameter (see Table I) was defined as the starting point. Additionally, a literature study was conducted to cover the state-of-the-art parameter ranges for the sensitivity studies, which are also listed in Table II. Two groups are defined to cover the sensitivity of  $E_{loss}$  on “anode” side and “cathode” side. Because of parameters with high impact on the QoI, it is difficult to determine the sensitivity for parameters with low impact on the QoI, since their sensitivity is hidden. Therefore, the proposed grouping is helpful to receive useful results for all analyzed input parameters.<sup>54</sup> For each group, two sensitivity studies are carried out as listed on the right-hand part of Table II.

Study A+ captures the sensitivity of the QoI, for an improvement of all input parameters relating to the “anode” side group based on the reference parameterization. The entries min and max in Table II define the lower and upper boundaries for each input parameter. Analogous to this, study A– addresses the deterioration of input parameters from the “anode” side group in relation to the reference case. For the “cathode” group of input parameters, the sensitivity studies C+ and C– are defined and carried out in the same way as described for the “anode” side group.

For the following process steps in Fig. 2, the MATLAB toolbox UQLab was used for calculating the mathematical surrogate models and the realization of the different sensitivity studies.<sup>55</sup> Training data needs to be generated to get one surrogate model for each sensitivity study. First, latin hypercube sampling was used to generate input vectors for each study, which ensured the variation of each parameter over the entire specified range according to Table II. In other words, one input vector contains one value for each parameter inside the specified parameter range for the respective study. For the “anode” side group, 120 different input vectors were used for each study to perform 120 p2D model evaluations. The results for  $E_{loss}$  from the p2D model along with the corresponding input vector were defined as the training dataset with a size of 120. For the “cathode” side sensitivity studies, a reduced number of 60 full p2D model evaluations lead to a sufficient training dataset, since only three input parameters were varied. Afterwards, gaussian processing was applied to calculate a mathematical surrogate model for  $E_{loss}$ . The reliability of each surrogate model to predict  $E_{loss}$  was tested by using a verification dataset of size 10, which was not part of the training dataset. For each study, the deviation between the p2D and the surrogate results was analyzed by calculating the relative and the absolute root mean squared error (RMSE) for  $E_{loss}$ , which are presented in Table III. With a relative RMSE <2%, all surrogate

**Table III.** Verification of the surrogate models for each sensitivity study. Randomly selected input vectors of size 10, which were not part of the training dataset, were applied to calculate  $E_{loss}$  with the p2D and the surrogate models. The results were used to calculate the absolute and relative RMSE of  $E_{loss}$  between the p2D and the surrogate model results. The cell was discharged with the specified CCCV protocol (CC: 1C, CV: 2.8 V, cutoff current: C/100).

Study type	RMSE/m Wh m <sup>-2</sup>	RMSE relative/%
A+	45.26	0.41
A-	23.44	0.12
C+	50.10	0.32
C-	365.56	1.70

models provided results close to the p2D models, which is considered to be sufficient for a meaningful interpretation of the results of the sensitivity study.

Subsequent to the verification of the surrogate models, the first-order and total-order Sobol' indices were calculated from  $n = 10,000$  surrogate model evaluations using Monte-Carlo simulation. The first-order and total Sobol' indices are calculated by UQLab. The formulae can be found online in the documentation.<sup>55</sup>

## Results and Discussion

**Overpotential analysis.**—To analyze the impact of SPE interlayers and coatings on the ASSB performance, first the overpotential analysis introduced in the previous section was conducted for the reference parameterization. Figure 3 illustrates the seven contributions to the total overpotential calculated according to Table A-II for the simulation of a 1C constant-current (CC) discharge to the cutoff voltage  $U_{cell,end} = 2.8$  V. The red dashed line depicts the open circuit voltage (OCV)  $U_{eq}$  of the cell in equilibrium and the black dashed line represents the cell voltage between the terminals during discharge. The area between the OCV and the cell voltage  $U_{cell}$  shows the total overpotential, resulting directly from numerical simulation. The separated colored areas represent the individual shares of overpotential and were calculated analytically according to Table A-II. The sum of shares almost perfectly fills the area between the OCV  $U_{eq}$  and the cell voltage  $U_{cell}$ , which can be seen as an indicator for plausible results.

First, the dominant polarization effects are described and discussed. The gray-coloured area in Fig. 3 represents the overpotential caused from electrophoretic transport in the LLZO phase within the composite cathode. Striking here is the linear increase of overpotential with ongoing discharge. This behavior is caused by a reaction front regarding the intercalation process of Li ions into the AM. Due to the low ionic conductivity in LLZO compared to the assumed high electronic conductivity in the composite cathode, Li ions tend to use the shortest path in the ionic-conductive LLZO phase before intercalating into the AM phase. Therefore, as soon as the AM near the separator is fully lithiated, the reaction front starts to move uniformly through the cathode domain. This results in an increased pathlength for Li ions in the LLZO phase and a linear increase in overpotential. This effect is already known for liquid electrolyte cells and discussed by Srinivasan et al.<sup>60</sup> Since this effect is less related to the scope of polymer interlayers, a further discussion is not presented in this study.

The blue area in Fig. 3 represents the overpotential due to the charge transfer at the SPE|LLZO interface at  $x = x_1$  (see Fig. 1). During 1C discharging, the overpotential  $\Delta\phi_{if}$  remained constant at 178 mV. Corresponding to Eq. 7,  $\Delta\phi_{if}$  is dependent on the electrolyte potentials in the SPE interlayer and the LLZO separator, respectively. Since  $t_{+,LLZO}$  equals one in the LLZO phase, no Li-ion concentration gradients occurred. Therefore, the Li-ion concentration at the SPE|LLZO interface remained constant and did not impact the charge transfer overpotential at  $x = x_1$ . The influence of

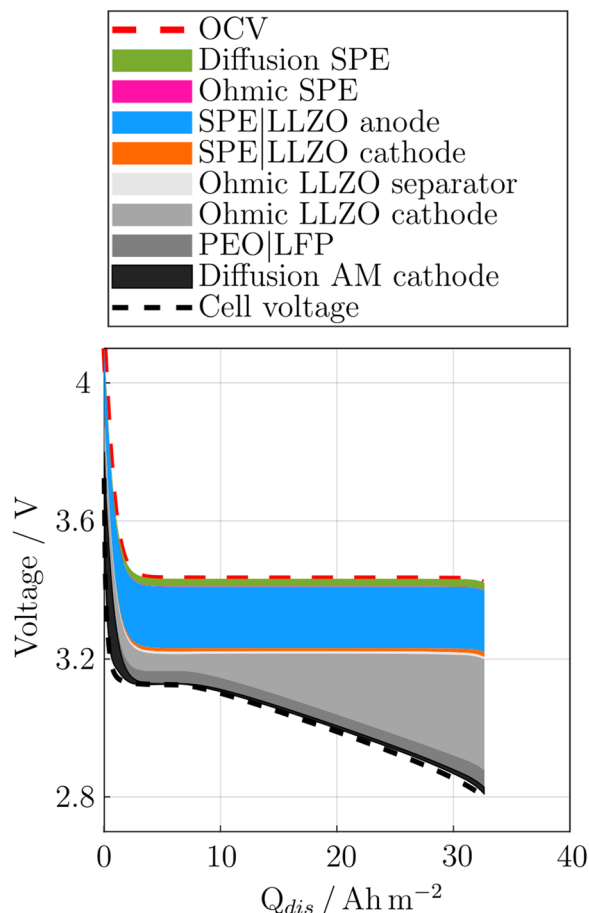


**Figure 3.** Overpotential analysis of the p2D 1C discharge simulation results, using the reference parameterization according to Table I. The cell was discharged until the cell voltage (dashed black line) reached  $U_{cell} = 2.8$  V. The total cell overpotential (difference between OCV and cell voltage) is split into its respective parts according to the calculations after Nyman et al. (see Table A-II).<sup>48</sup>

concentration gradients on the SPE|LLZO interface kinetic was considered with a concentration-dependent exchange current density  $i_{0,if}$  as listed in Table I. Starting at the SPE Li-ion equilibrium concentration of  $1960 \text{ mol m}^{-3}$  the Li-ion concentration at  $x = x_1$  decreased to a steady-state value of  $1857 \text{ mol m}^{-3}$ , which lead to a decrease in exchange current density of less than 2.8%. For the chosen parameterization, the effect of concentration-dependent interface kinetics is negligible regarding the overpotential analysis. Nevertheless, it should be mentioned that the impact of concentration-dependent kinetics could be more severe for a different combination of materials, a different Li-ion reference concentration, or high-rate discharging procedures.

The overpotential due to the charge transfer between the SPE coating on the LFP-AM particles and the LLZO electrolyte in the composite cathode is represented by the orange area in Fig. 3. Compared to the SPE anode interlayer, a small overpotential of 10 mV was calculated for the charge transfer at the SPE|LLZO interface in the composite cathode. The significant lower polarization can be explained with the lower local current density for the charge transfer due to the porous electrode structure and the small particle radius.

Last, the overpotential due to the ionic transport in the  $5 \mu\text{m}$  thick SPE interlayer is discussed in the following paragraph. Ionic transport in the SPE interlayer can occur due to migration and diffusion. The overpotential due to diffusion in the SPE phase was calculated with 22 mV, whereas only 1.4 mV of overpotential arose from Li ion transport by migration.



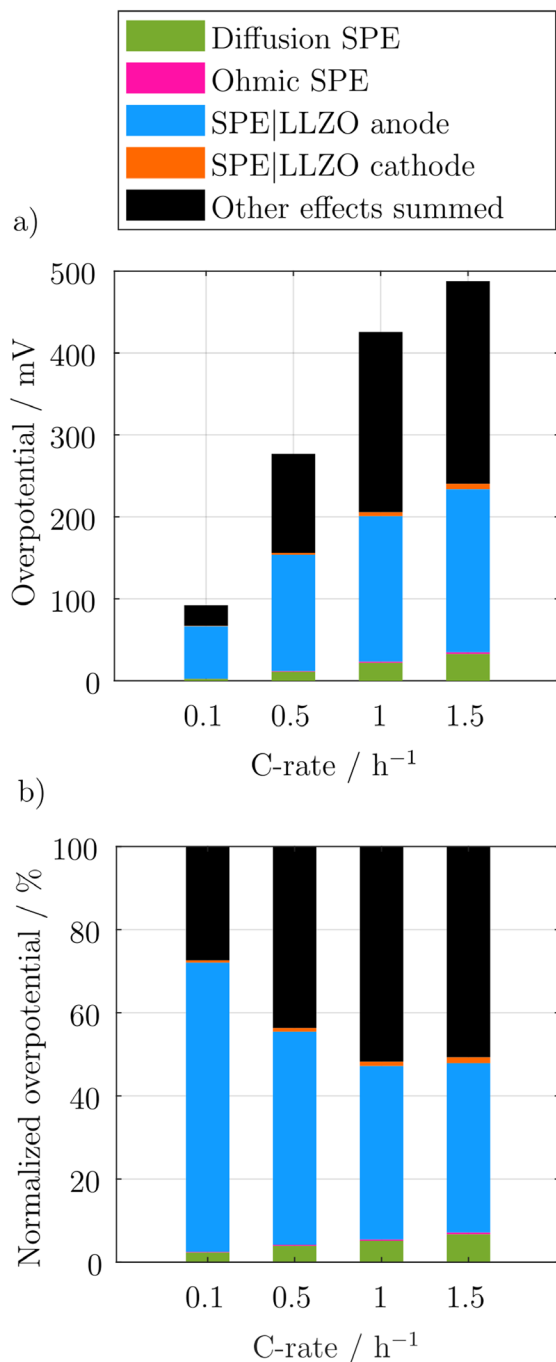


**Figure 4.** Analysis of the mean overpotential of the CC discharge simulations at 0.1C, 0.5C, 1C, and 1.5C using the reference parameterization according to Table I. In (a), the height of each bar shows the total mean overpotential at the given C-rate. Only the SPE-related contributions are presented separately and overpotential contributions from other effects were summed up and visualized by the black part of each bar. In (b), the single contributions to the normalized total overpotential are presented.

The overpotential analysis shows that the charge transfer kinetics at the SPE|LLZO interface significantly contribute to the total polarization. Ohmic losses in the solid electrolyte are the second major contributor, but are not related to the SPE interlayer.

More generally, by assuming similar interface kinetics between the SPE and different ISEs, the importance of further studying the SPE interlayer becomes clear from these results. The interlayer comes with advantages, as discussed in the introduction, but

introduces further overpotentials at the interface, which need to be taken into account when considering the cell performance.

Figure 4 allows for a closer inspection of the individual overpotential contributions at different operational conditions. The mean overpotentials during discharge are presented in dependence on the C-rate, between 0.1C and 1.5C. Figures 4a and 4b show the mean absolute and mean relative overpotentials, respectively. To focus on the impact of the polymer interlayer and its related effects, the remaining contributions are grouped and labeled as “Other effects summed”.

For 0.1C, solely the overpotential due to charge transfer at the SPE|LLZO interface at  $x = x_1$  (blue) and the ohmic overpotential due to migration in the LLZO phase in the cathode (black) dominate the total polarization. With increasing C-rate, the total overpotential increases non-linearly with slightly decreasing slope, since all charge transfer processes are represented with a BV-like kinetic. Therefore, the charge transfer processes get more efficient with increasing C-rates. This can be seen more clearly from the blue area in Fig. 4b. The relative overpotential contribution from the SPE|LLZO charge transfer decreased significantly with increasing C-rate up to 1C. Another factor influencing the SPE|LLZO charge transfer overpotential is the exchange current density  $i_{0,if}$ , which decreases by 4% at 1.5C compared to the initial value in equilibrium state due to the decrease of Li-ion concentration. Interestingly, it should be noted that this process is reversed for the charging scenario, where an improvement of exchange current density is expected due to increased Li-ion concentration at the SPE|LLZO interface. The charge transfer overpotential at the SPE|LLZO interface in the composite cathode (orange) remained smaller than 3% with increasing current.

Additionally, the relative diffusive share of total overpotential in the SPE domain, represented with the green-coloured face in Fig. 4b, increased noticeably from 2.4% to 6.7%, comparing the 0.1C and 1.5C discharge. This can be explained by a slightly non-linear increase in concentration gradient and related changes of Li-ion concentration-dependent transference number  $t_{+,SPE}$ , thermodynamic factor  $TDF_{SPE}$ , and Diffusivity  $D_{SPE}$ . Last, the contribution from ohmic polarization due to migration in the SPE domain, colored pink in Fig. 4b, did not increase significantly for higher C-rates.

From the polarization analysis, it can be concluded that two dominant effects caused the largest part of total overpotential for the concentration-dependent reference parameterization, namely the charge transfer overpotential at the SPE|LLZO interface at  $x = x_1$  and the Li-ion migration in the LLZO phase in the composite cathode. Furthermore, an evaluation of the C-rate dependency of overpotentials showed that the share of total polarization from the SPE|LLZO interfacial charge transfer decreased with increasing C-rates due to improved charge transfer kinetics. Nevertheless, the incorporation of a thin SPE interlayer with a thickness of 5  $\mu\text{m}$  lead to large additional overpotentials, which were mainly caused by the charge transfer at the SPE|LLZO interface. To cover the interdependencies between SPE-related model input parameters and output more generally, as well as to identify potentials to optimize ASSB cell performance, the parameter range that the literature provides has to be considered. We expect that the presented results can differ dependent on the material combination at the SPE/ISE interface, microstructure and morphology of the composite cathode, as well as in dependence of the AM. In the following, the results of the performed global sensitivity studies, as introduced in the modeling section, will cover variations of model input parameters and their influence on the model output sensitivity. From this, a general discussion of the impact of polymer interlayers on cell performance is presented.

**Sensitivity analysis.**—Based on the process mentioned above for realizing the global sensitivity analysis in Fig. 2, the results of the sensitivity of the chosen QoI parameter  $E_{loss}$  with varying polymer-

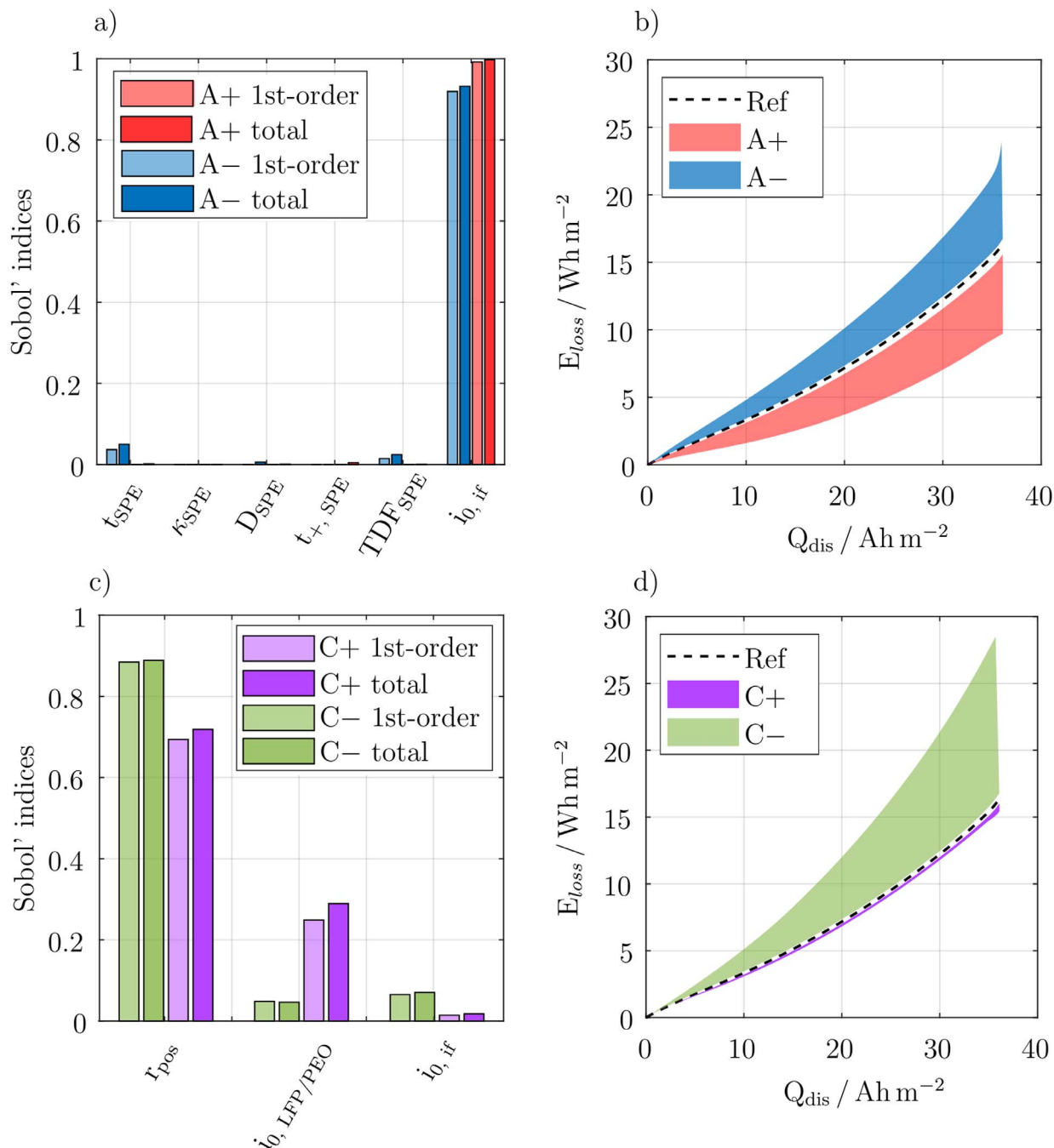


**Figure 5.** Results of the global sensitivity studies presented in Table II. In (a) and (c), the 1st-order and total order Sobol' indices are presented. In (b) the transient behavior of  $E_{loss}$  during CCCV discharge (CC: 1C, CV: 2.8 V, C/100 cutoff) is presented for the reference parameterization (dashed black line), for the improvement (A+), and the deterioration (A-) of input parameters on “anode” side. The multiple combinations of input parameters during the sensitivity studies lead to a spread of  $E_{loss}$ , which is represented by the coloured areas for better clarity. The theoretical energy content of the cell  $E_{th}$  is equal to  $123.5 Wh m^{-2}$ . The transient behavior of  $E_{loss}$  for the sensitivity studies of “cathode” is presented in (d).

related input parameters are presented and discussed in Fig. 5. In a) and b), the results for the “anode” side parameters are presented, in c) and d), the “cathode” side sensitivity studies are evaluated. The coloring distinguishes input parameter improvement or deterioration according to the defined study as presented in Table II.

The first-order and total Sobol' indices for “anode” side-related input parameters, were calculated on the basis of 10,000 surrogate model evaluations. Since the Sobol' indices were calculated separately for each study, statements about the sensitivity of the QoI can only be made within each study, but a comparison of the results between the different studies is not possible. Therefore, additional

analysis of the absolute changes of  $E_{loss}$  was needed to draw conclusions on model output sensitivity across all studies. For this, the transient behavior of the output variable  $E_{loss}$ , was analysed. In detail, the transient behavior of  $E_{loss}$  was obtained from the training datasets and plotted over the discharged capacity. A constant-current-constant-voltage (CCCV) discharge profile with a CC rate of 1C until 2.8 V and a C/100 current cutoff in the constant-voltage (CV) phase was applied to reach the same discharge capacity end point, for each simulation. The black dotted line depicts the course of  $E_{loss}$  for the reference parameterization, which was already discussed in terms of polarization analysis in the previous section.

For each of the varied input parameters in Fig. 5a, the red colored bars represent the Sobol' indices for study A+, as well as the blue bars do for study A−, respectively. For both studied cases, the Sobol' indices calculated for the exchange current density at the SPE|LLZO interface  $i_{0,if}$  were close to 1. Qualitatively, this means that nearly the total variance of the QoI  $E_{loss}$  is caused by the variation of  $i_{0,if}$ . An improvement or a deterioration of the SPE bulk transport parameters, within the given literature range presented in Table II, did not affect  $E_{loss}$  significantly. The mean overpotentials caused by Li-ion SPE bulk transport did not change noticeable compared to the reference parameterization. It should be highlighted that the statements regarding the sensitivity on SPE bulk parameters might be valid for thin polymer interlayers like in this analyzed cell setup. This can be expected due to a measurable contribution to the variance of  $E_{loss}$  of 5% for the total Sobol index of the SPE layer thickness  $t_{SPE}$ . Since this study is focused on SPE interlayers and coatings, an investigation of a SPE layer thickness  $t_{SPE} > 10 \mu\text{m}$  was not considered useful regarding its practical relevance. Figures 5c and 5d present the results for the first-order and total Sobol' indices and the transient behavior of  $E_{loss}$  for the “cathode” related studies, respectively. The analysis of the transient behavior showed a strong scattering of  $E_{loss}$  for study C−, represented by the green-colored face. The worst case scenario lead to an increase of  $E_{loss}$  at EoD to  $28 \text{ Wh m}^{-2}$  resulting in a maximum spread at EoD of  $12 \text{ Wh m}^{-2}$ . Together with the information from the Sobol indices in Fig. 5c it can be stated, that the increase of the LFP-AM particle radius  $r_{pos}$  up to  $5 \mu\text{m}$  caused 90% of the variance of  $E_{loss}$ , as can be seen from Sobol' indices of 0.9. Since the change of particle radius has an influence on several physics-related effects, a detailed discussion is provided in the following.

A change of the particle radius  $r_{pos}$  leads to a change of the specific surface area since the AM volume fraction  $\epsilon_{AM}$  was kept constant for the entire study. The specific surface defines the area at which the charge transfer between PEO and LFP occurs, and the Li ions have to cross the SPE|LLZO interface. The specific surface area is inversely proportional to  $r_{pos}$ , which leads to a decrease in specific surface area with increasing  $r_{pos}$ . This in turn results in an increased local current density at the interface. Due to the BV-like kinetics for charge transfer between SPE and LFP, as well as for charge transfer at the SPE|LLZO interface (see Eq. 8), an increase of local current density leads to an increase of charge transfer overpotential. Additionally, a larger  $r_{pos}$  leads to an increase of Li-ion concentration gradients, which results in larger diffusion-related overpotentials.

This is clarified by the following description regarding the evolution of charge transfer overpotentials in the composite cathode due to an increase of  $r_{pos}$ . To do this, the charge transfer overpotentials were calculated for the worst-case scenario, causing the highest losses according to Fig. 5d, and compared to the overpotentials due to the reference parameterization. Regarding the charge transfer at the SPE|LLZO interface at the LFP-AM surface, the overpotential increased from 10 mV in the reference case to 102 mV in the worst-case scenario by a factor of approx. 10. The overpotential from the SPE/LFP charge transfer increased from 43 mV to 120 mV. In conclusion, the polarization which arose from an SPE coating depends on the specific surface area and the local current distribution in the composite cathode and could lead to a limiting performance of the cell due to large charge transfer overpotentials. The variation of  $r_{pos}$  revealed this dependence. Still, more parameters describing the microstructure like the tortuosity  $\tau$  and the combination of active material fraction  $\epsilon_{AM}$ , SE material fraction  $\epsilon_{SE}$  and void space also have an influence on current distribution in the composite cathode.

Furthermore, the strong sensitivity of  $r_{pos}$  represented by Sobol' indices of 0.9 is also influenced by the aforementioned reaction front since it leads to an increase of local current densities. To bring this in a generally valid perspective, with the usage of an AM having an OCV with a steeper slope, for example a nickel-rich AM, the reaction front effect is expected to be minor. Therefore, a more homogeneous current distribution in the composite cathode is

expected and could result in a reduced sensitivity of  $r_{pos}$  (lower Sobol indices) and an increased sensitivity on the exchange current density  $i_{0,if}$  (higher Sobol indices).

Compared to the deterioration of input parameters in study C−, the improvement of “cathode” side related parameters in study C+ did not result in a significant reduction of  $E_{loss}$ , which could be derived from the small magenta-colored face in Fig. 5d.

**Optimization potential.**—The four conducted sensitivity studies disclose two dominant input parameters with the exchange current density at the SPE|LLZO interface  $i_{0,if}$  for “anode” side studies and the LFP-AM particle radius  $r_{pos}$  for “cathode” side, respectively. Figure 6 shows the dependence of the QoI  $E_{loss}$  on  $i_{0,if}$  in (a) and on  $r_{pos}$  in (b). The plotted raw data of  $E_{loss}$  result from the 10,000 surrogate model evaluations. Therefore, each circular marker presents one value of  $E_{loss}$ , due to different combinations of input parameters within the considered parameter range according to Table II.

Identifying the dependence between the dominant input parameters and  $E_{loss}$  is helpful to disclose optimization potentials regarding the ASSB cell performance. As depicted in Fig. 6a, an exponential-like decay of  $E_{loss}$  could be observed with increasing values for the exchange current density  $i_{0,if}$ . Since  $i_{0,if}$  is a pre-exponential factor the BV equation (see Eq. 1), less overpotential  $\Delta\phi_{if}$  is needed to drive the total current  $i_{if}$  with increasing values for the exchange current density  $i_{0,if}$ . With increasing  $i_{0,if}$  only minor improvements regarding the reduction of  $E_{loss}$  could be achieved. The exchange current density  $i_{0,if}$  is a material property and depends on the contact materials at the interface and can be determined by measuring the charge transfer resistance  $R_{ct,if}$  (Eq. 2). As previously discussed in the modeling section, a power law proportionality of  $R_{ct,if}$  to the Li-salt concentration in the SPE is known (Eq. 3) from literature. Therefore, the identified correlation presented in Fig. 6a could be useful to define a value for  $i_{0,if}$  for the trade-off between permissible overpotential and improvement of  $i_{0,if}$ .

As expected from previous results in Fig. 5, the potential to reduce  $E_{loss}$  with  $r_{pos} < 1 \mu\text{m}$  was minor, as highlighted by the course of the magenta-colored area in Fig. 6b. Interestingly, the green-colored data points from study C− disclose the impact of the additionally varied kinetic parameters  $i_{0,if}$  and  $i_{0,LFP/PEO}$ . Their impact on  $E_{loss}$  can be seen from the spread in  $E_{loss}$  at a given particle radius. For  $r_{pos} = 1 \mu\text{m}$ , the maximum spread is  $2.13 \text{ Wh m}^{-2}$ , which increased to from  $16.5 \text{ Wh m}^{-2}$  to  $5.86 \text{ Wh m}^{-2}$  for  $r_{pos} = 5 \mu\text{m}$ . The maximum spreads in  $E_{loss}$  correspond to an increase of 12.9% and 24.4%, respectively, when the smallest value for  $E_{loss}$  at the respective particle radius is considered to be the baseline value. This can be explained again with the reduction of specific surface area with increasing  $r_{pos}$  and the BV equation. With a lower specific surface area and the same value for the exchange current density, higher overpotentials and therefore higher  $E_{loss}$  resulted.

This trend leads to the question if an improvement of the exchange current densities  $i_{0,if}$  and  $i_{0,AM,r_{pos}}$  can lead to a reduction of  $E_{loss}$  for a AM particle size  $r_{pos} > 1 \mu\text{m}$ . The black line in Fig. 6b represents  $E_{loss}$  when only the particle radius is increased, but the best-case kinetics are used, which corresponds to the maximum values for the exchange current densities given in Table II. The lower slope of the black line compared to the slope of the green colored-area with increasing particle radius indicates that an improvement of kinetics is more relevant for larger AM particles. But nevertheless, the increase of the AM particle radius  $r_{pos}$  still leads to an increase of  $E_{loss}$ . In conclusion, the thin SPE coating of LFP-AM particles shows a minor impact on polarization losses if the particle radius is below  $1 \mu\text{m}$  and the exchange current density  $i_{0,if}$  at the SPE|LLZO interface is at least around  $1 \text{ A m}^{-2}$ . For larger particles, the impact of SPE|LLZO charge transfer kinetics increased compared to smaller particles, but  $E_{loss}$  is still dominated by the particle radius  $r_{pos}$ .

The results shown so far discussed the impact of SPE interlayers and SPE AM particle coatings based on a reference parameterization,

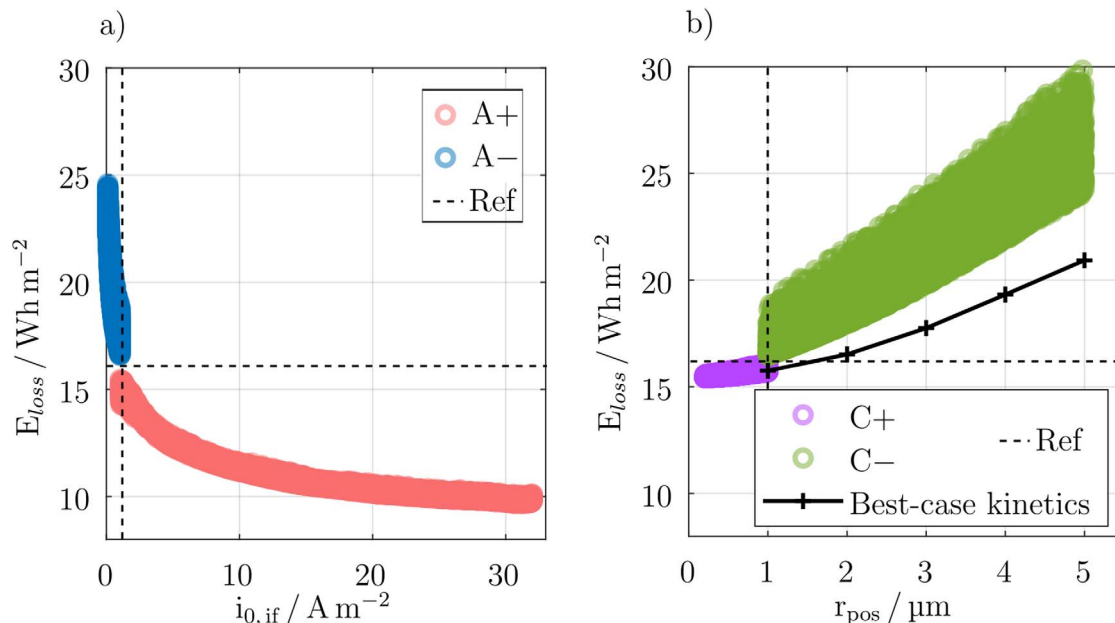


**Figure 6.** Dependence of  $E_{loss}$  on the variation of the exchange current density at the SPE|LLZO interface  $i_{0,if}$  in (a) and on the variation of AM particle radius  $r_{pos}$  in (b). Each data point presented by a circular marker represents a different combination of input parameters, leading to varying results for  $E_{loss}$  during the Monte-Carlo simulations in the sensitivity studies. In (b), the solid black line depicts the dependence of  $E_{loss}$  on  $r_{pos}$ , if the maximum values for the exchange current densities  $i_{0,if}$  and  $i_{0,LFP|PEO}$  (see Table II) were applied.

which covers the state of the art, and disclosed the most impactful input parameters  $i_{0,if}$  and  $r_{pos}$ , as well as their potential to improve  $E_{loss}$  compared to the reference cell parameterization. Based on these results, the potential for improvement of the rate-capability behavior due to the improvement of the most impactful parameters reveals more information on the practical relevance of solid-state cells with SPE interlayers and coatings. To investigate these improvements, Fig. 7 shows the normalized discharged capacity that can be achieved with three different options of improvement: An improved cathode particle radius of  $r_{pos} = 200$  nm; an improved exchange current density at the LLZO/SPE interface of  $i_{0,if} = 32 \text{ A m}^{-2}$ ; and an idealized battery design without any SPE interlayers contributions. The results of simulations without SPE interlayers represent the idealized maximum performance that can be achieved based on the given cell design. However, in practice, as mentioned in the introduction, various side effects such as interphase formation, void formation, and potential cracking of AM particles can significantly affect the rate capacity.

As expected, the model cell parameterized with the reference parameterization showed the worst rate capability. Strong capacity fading already started at 1C leading to a decreased accessible discharge capacity of 90% at 1C, 41% at 2C and 17% at 3C. In comparison, using the identical parameterization for the model cell, but excluding the SPE interlayer on “anode” side and the SPE coating on “cathode” side, the accessible discharge capacity increased to 96% at 1C, 73% at 2C, and 48% at 3C. Together with the results of Fig. 3, the large overpotential contribution from the charge transfer at the SPE|LLZO interface is identified as a rate-limiting effect. The rate limitation could be reduced by an improvement of the dominant parameters  $i_{0,if}$  and  $r_{pos}$ . Compared to the reference parameterization, a reduction of  $r_{pos}$  to 200 nm leads to an increase of accessible discharge capacity from 90% to 96% at 1C, which is the same result compared to the cell without SPE interlayers and coatings. The improvement of the exchange current density to  $i_{0,if} = 32 \text{ A m}^{-2}$  leads to a significant improvement of rate capability even at the highest tested discharge rates. At 2C, the accessible capacity increased from 41% to 61% and at 3C from 17% to 35%, compared to the reference case. With this, we want to emphasize that an improvement of charge transfer kinetics at the interface between SPE|LLZO could significantly reduce the overpotential and improve

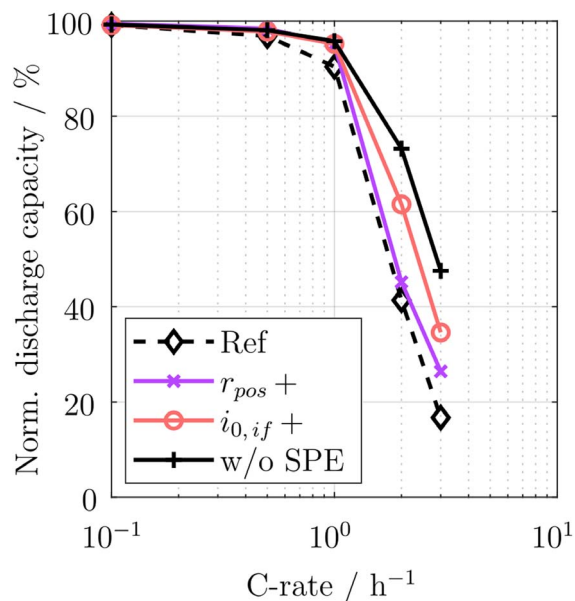


**Figure 7.** CC rate capability of the model cell with SPE interlayer and SPE AM particle coating achieved with the reference parameterization, for the reduction of the sensitive AM particle radius to  $r_{pos} = 200$  nm, marked as  $r_{pos} +$ , as well as for the improvement of the dominant exchange current density to  $i_{0,if} = 32 \text{ A m}^{-2}$ , marked as  $i_{0,if} +$ . The rate capability for the reference parameterization under idealized assumptions, without SPE interlayer and coating, marked as w/o SPE, was evaluated for comparison.

the rate capability of a cell containing additional SPE interlayers. Therefore, we encourage future work to find suitable SE material combinations with a low intrinsic interface charge transfer resistance.

## Conclusions

The impact of ionically conductive SPE interlayers on ASSB cell performance was evaluated using a model-based overpotential



characterization and a global sensitivity analysis. The p2D model approach was used and extended to account for ionic transport in SPE interlayers and kinetics for the charge transfer at the SPE|LLZO interface to represent the properties of SPE interlayers. Charge transfer at the SPE|LLZO interface was considered with a BV-like kinetic and a Li-ion concentration-dependent exchange current density. With the presented model, the influence of an SPE interlayer in contact with a Li-metal anode and of an SPE AM-surface coating in the composite cathode was investigated.

The performed overpotential analysis for a literature-based reference parameterization revealed a significant contribution from the charge transfer at the SPE|LLZO interface in contact with the anode, which amounts to 178 mV and a relative share of 42% in relation to the total overpotential at a 1C discharge. Interestingly, a 20-fold lower SPE|LLZO interface charge transfer overpotential was observed for the SPE AM particle coating in the composite cathode. This could be explained by small local current densities in the composite cathode due to a large AM particle surface area. Additionally, a negligible overpotential contribution that arose from ionic transport in the bulk SPE was observed in this study. Due to the S-shaped BV-like kinetics at the SPE|LLZO interface, the efficiency of charge transfer increased with increasing discharge rate, reducing the relative overpotential contribution. As an outlook, the impact of the SPE interlayer might be of particular relevance for parameterizations that do not show a reaction front effect during (de) lithiation since the increase in ohmic overpotential inside the ISE with ongoing (dis)charge might be reduced. Assuming that the ionic conductivity of LLZO is sufficiently high, the total overpotential could be dominated solely by the charge transfer at the SPE|ISE interface.

The global sensitivity analysis and the subsequent evaluation of the variance-based Sobol' indices revealed the exchange current density  $i_{0,if}$  and the AM particle radius  $r_{pos}$  as the polymer-related

input parameters with the highest impact on cell performance. An exponential-like decay was observed for the output parameter  $E_{loss}$  with increasing exchange current density  $i_{0,if}$ . This analysis method should be helpful to define a trade-off between permissible overpotential and improvement of dominant parameters. Finally, the simulation a rate-capability test disclosed that the accessible capacity of ASSB cells can be strongly deteriorated for discharge rates  $>1C$ , due to the incorporation of polymer interlayers. Furthermore, the rate-capability of the ASSB model cell could be improved significantly by an improvement of the SPE|ISE interface kinetics.

This motivates further research of material experts to find material combinations of SEs with a low charge transfer resistance and simultaneously maintain advantages that could arise from using two different SEs. Additionally, concepts to increase the surface area between the SPE interlayer and the LLZO separator should be evaluated to significantly reduce overpotential contribution. Furthermore, the methods used in this study should be considered for the design of hybrid SEs.

### Acknowledgments

This research is partially funded by the Bavarian Ministry of Economic Affairs, Regional Development and Energy within the research project "Industrialisierbarkeit von Festkörperelektrolytzellen" as well as by the German Federal Ministry of Education and Research (BMBF) under grant number 03XP0184I (ProFeLi). The authors are thankful for fruitful discussions with the members of the TUMint Energy Research GmbH and the consortium of the "ProFeLi" project.

### Appendix

**Table A-I. Differential equations of hybrid model.**

<b>Li</b>	Potentials	$\Phi_s = 0$
	Kinetics	$i_{loc}(x, t) = i_0(x, t) \left[ \exp\left(\frac{a_a F \eta(x, t)}{R T}\right) - \exp\left(-\frac{a_c F \eta(x, t)}{R T}\right) \right] \Big _{x=x_0}$
<b>SPE</b>	Conservation of mass	$\frac{\partial c_{Li, SPE}(x, t)}{\partial t} = \frac{\partial}{\partial x} \left( D_{Li, SPE} \frac{\partial c_{Li, SPE}(x, t)}{\partial x} + \frac{i_{SPE}(x, t) t_+^{SPE}}{F} \right)$
	Conservation of charge	$\frac{\partial i_{SPE}(x, t)}{\partial x} = 0$
	Potentials	$\frac{\partial \Phi_{SPE}(x, t)}{\partial x} = -\frac{i_{SPE}(x, t)}{\kappa_{SPE}} + \frac{2 R T}{F} (1 - t_+^{SPE}) \left( 1 + \frac{d \ln f_{\pm}}{d \ln c_{Li, SPE}(x, t)} \right) \frac{\partial \ln c_{Li, SPE}(x, t)}{\partial x}$
<b>LLZO</b>	Conservation of mass	$\frac{\partial c_{Li, LLZO}(x, t)}{\partial t} = 0$
	Conservation of charge	$\frac{\partial i_{LLZO}(x, t)}{\partial x} = 0$
	Potentials	$\frac{\partial \Phi_{LLZO}(x, t)}{\partial x} = -\frac{i_{LLZO}(x, t)}{\kappa_{LLZO}}$
<b>Cathode</b>	Conservation of mass	$\frac{\partial c_{Li, LLZO}(x, t) \epsilon_{LLZO}}{\partial t} = 0$
		$\frac{\partial c_s(x, t, r)}{\partial t} = \frac{1}{r^2} \frac{\partial}{\partial r} \left( D_s r^2 \frac{\partial c_s(x, t, r)}{\partial r} \right)$
	Conservation of charge	$\frac{\partial i_{LLZO}(x, t)}{\partial x} + \frac{\partial i_s(x, t)}{\partial x} = 0 \quad \text{with} \quad \frac{\partial i_s(x, t)}{\partial x} = -\frac{3 \epsilon_s}{r_p} i_{loc}(x, t)$
	Potentials	$\frac{\partial \Phi_{LLZO}(x, t)}{\partial x} = -\frac{i_{LLZO}(x, t)}{\kappa_{LLZO}^{eff}}$
		$\frac{\partial \Phi_s(x, t)}{\partial x} = -\frac{i_{app}(t) - i_{LLZO}(x, t)}{\sigma_s^{eff}} \quad \text{with} \quad i_{app}(t) = i_s(x, t) + i_{LLZO}(x, t) \quad \forall x, t$
	Kinetics	$i_{loc}(x, t) = i_0(x, t) \left[ \exp\left(\frac{a_a F \eta(x, t)}{R T}\right) - \exp\left(-\frac{a_c F \eta(x, t)}{R T}\right) \right]$

**Table A-II. Calculation of single overpotential contributions for the model cell design in Fig. 1, adapted from Nyman et al.<sup>48</sup>**

Total current density	$i_{tot} = \int_{x_0}^{x_1} a i_{loc} dx = i_{app}$
<b>Domain</b>	
Diffusion overpotential SPE phase	$\frac{1}{i_{tot}} \int_{x_2}^{x_3} \frac{2 RT}{c_{Li, SPE} F} \left( 1 + \frac{\partial \ln f_{\pm}}{\partial \ln c_{Li, SPE}} \right) (1 - t_+) \frac{\partial c_{Li, SPE}}{\partial x} i_{SPE} dx$
Diffusion overpotential AM particle	$\frac{1}{i_{tot}} \int_{x_2}^{x_3} a i_{loc} (U_{eq, surf} - U_{eq, ave}) dx$
Ohmic overpotential SE phase	$\frac{1}{i_{tot}} \int_{x_1}^{x_2} \frac{i_{LLZO}^2}{\kappa_{eff}} dx$
Ohmic overpotential AM phase	$\frac{1}{i_{tot}} \int_{x_2}^{x_3} \frac{i_s^2}{\sigma_{eff}} dx$
Charge transfer reaction overpotential Cathode	$\frac{1}{i_{tot}} \int_{x_1}^{x_2} a i_s (\phi_s - \phi_{LLZO} - \Delta \phi_{phB, AM} - U_{eq, surf, AM}) dx$
<b>Boundary</b>	
Charge transfer reaction overpotential Anode	$(\phi_{Li} - \phi_{SPE} - U_{eq, surf, Li}) _{x=x_0}$
Charge transfer overpotential PEO LLZO	$(\phi_{LLZO} - \phi_{SPE}) _{x=x_1}$

**Table A-III. Minimal information set to enable verifiable theoretical battery research according to Mistry et al.<sup>61</sup>**

Manuscript Title:	Impact of Polymer Interlayers on All-Solid-State Battery Performance Using a Physicochemical Modeling Approach	
Submitting Author: <sup>a)</sup>	Maximilian Scheller	
# Question		Y—N—NA <sup>b)</sup>
1	Have you provided all assumptions, theory, governing equations, initial and boundary conditions, material properties (e.g., open-circuit potential) with appropriate precision and literature sources, constant states (e.g., temperature), etc..?	Y
<b>Remarks:</b>		
2	If the calculations have a probabilistic component (e.g., Monte Carlo, initial configuration in Molecular Dynamics, etc..), did you provide statistics (mean, standard deviation, confidence interval, etc...) from multiple (3) runs of a representative case?	Y
<b>Remarks:</b>	The deviation of the surrogate model (reduced-order) results compared to p2D model results is presented in Table 3 by the absolute and relative RMSE.	
3	If data-driven calculations are performed (e.g., machine learning), did you specify dataset origin, the rationale behind choosing it, what information it contains, and the specific portion of it being utilized? Have you described the thought process for choosing a specific modeling paradigm?	NA
<b>Remarks:</b>		
4	Have you discussed all sources of potential uncertainty, variability, and errors in the modeling results and their impact on quantitative results and qualitative trends? Have you discussed the sensitivity of modeling (and numerical) inputs such as material properties, time step, domain size, neural network architecture, etc... where they are variable or uncertain?	Y
<b>Remarks:</b>	The evaluation and discussion of model-output uncertainty due to input parameter variation is the key section of this study. There is no discussion of mesh resolution or numerical error tolerances.	
5	Have you sufficiently discussed new or not widely familiar terminology and descriptors for clarity? Did you use these terms in their appropriate context to avoid misinterpretation? Enumerate these terms in the “Remarks”.	Y
<b>Remarks:</b>	All Symbols, Subscripts and Abbreviations are explained and introduced in the manuscript and listed on the list of symbols	

a) I verify that this form is completed accurately in agreement with all co-authors, to the best of my knowledge. b) Y the question is answered completely. Discuss any N or NA response in “Remarks”.

## ORCID

M. Scheller  <https://orcid.org/0000-0001-9495-9711>A. Durdal  <https://orcid.org/0000-0002-0479-5491>A. Frank  <https://orcid.org/0000-0001-8069-2948>J. Kriegler  <https://orcid.org/0000-0002-7961-7876>A. Jossen  <https://orcid.org/0000-0003-0964-1405>

## References

- G. E. Blomgren, *J. Electrochem. Soc.*, **164**, A5019 (2017).
- S. Randau et al., *Nat. Energy*, **5**, 259 (2020).
- M. Scheller, A. Aufschläger, A. Frank, M. Steinhardt, J. Sturm, and A. Jossen, *Journal of Energy Storage*, **56**, 105942 (2022).
- Y. Kato, S. Hori, T. Saito, K. Suzuki, M. Hirayama, A. Mitsui, M. Yonemura, H. Iba, and R. Kanno, *Nat. Energy*, **1**, 652 (2016).
- T. Famprikis, P. Canepa, J. A. Dawson, M. S. Islam, and C. Masquelier, *Nat. Mater.*, **18**, 1278 (2019).
- Y. Zhu, X. He, and Y. Mo, *CS applied materials & interfaces*, **7**, 23685 (2015).
- R. Ruess, S. Schweidler, H. Hemmelmann, G. Conforto, A. Bielefeld, D. Weber, J. Sann, M. Elm, and J. Janek, *J. Electrochem. Soc.*, **167**, 100532 (2020).
- R. Koerper, W. Zhang, L. de Biasi, S. Schweidler, A. O. Kondrakov, S. Kolling, T. Brezesinski, P. Hartmann, W. Z. Zeier, and J. Janek, *Energy & Environmental Science*, **11**, 2142 (2018).
- T. Shi, Y.-Q. Zhang, Q. Tu, Y. Wang, M. C. Scott, and G. Ceder, *J. Mater. Chem. A*, **8**, 17399 (2020).
- J.-M. Doux, H. Nguyen, D. H. Tan, A. Banerjee, X. Wang, E. Wu, C. Jo, H. Yang, and Y. Meng, *Adv. Energy Mater.*, **10**, 1452 (2020).
- J. Kasemchannan, S. Zekoll, D. S. Jolly, Z. Ning, G. Hartley, J. Marrow, and P. Bruce, *Nat. Mater.*, **18**, 1105 (2019).
- J. Schnell, T. Günther, T. Knoche, C. Vieider, L. Köhler, A. Just, M. Keller, S. Passerini, and G. Reinhart, *Journal of Power Sources*, **382**, 160 (2018).
- C. F. N. Marchiori, R. P. Carvalho, M. Ebadi, D. B. Brandell, and C. M. Araujo, *Chemistry of Materials*, **32**, 7237 (2020).
- S. Sen, E. Trevisanella, E. Niemiöller, B.-X. Shi, F. Simon, and F. Richter, *J. Mater. Chem. A*, **9**, 18701 (2021).
- S. Deng et al., *ACS Energy Lett.*, **5**, 1243 (2020).
- J. Kriegler, E. Jaimez-Farnham, M. Scheller, E. Dashjav, F. Konwitschny, L. Wach, L. Hille, F. Tietz, and M. Zaeh, *Energy Storage Materials*, **57**, 607 (2023).
- F. J. Simon, M. Hanauer, A. Henss, F. H. Richter, and J. Janek, *ACS applied materials & interfaces*, **11**, 42186 (2019).
- M. Weiss, F. Simon, M. R. Busche, T. Nakamura, D. Schröder, F. H. Richter, and J. Janek, *Electrochemical Energy Reviews*, **3**, 221 (2020).
- D. M. Pesko, Z. Feng, S. Sawhney, J. Newman, V. Srinivasan, and N. P. Balsara, *J. Electrochem. Soc.*, **165**, A3186 (2018).
- L. Stolz, G. Homann, M. Winter, and J. Kasnatscheew, *Mater. Today*, **44**, 9 (2021).
- I. Villaluenga, D. M. Pesko, K. Timachova, Z. Feng, J. Newman, V. Srinivasan, and N. P. Balsara, *J. Electrochem. Soc.*, **165**, A2766 (2018).
- A. Gupta and J. Sakamoto, *The Electrochemical Society Interface*, **28**, 63 (2019).
- F. Langer, M. S. Palagonia, I. Bardenhagen, J. Glenneberg, F. La Mantia, and R. Kun, *J. Electrochem. Soc.*, **164**, A2298 (2017).
- V. Wurster, C. Engel, H. Graebe, T. Ferber, W. Jaegermann, and R. Hausbrand, *J. Electrochem. Soc.*, **166**, A5410 (2019).
- M. Doyle, T. F. Fuller, and J. Newman, *J. Electrochem. Soc.*, **140**, 1526 (1993).
- M. Doyle and J. Newman, *Journal of Power Sources*, **54**, 46 (1995).
- J. Newman and N. P. Balsara, *Electrochemical systems* (Wiley, Hoboken, NJ) 4th ed. (2021).
- N. Wolff, F. Röder, and U. Krewer, *Electrochimica Acta*, **284**, 639 (2018).
- S. Toghyani, F. Baakes, N. Zhang, H. Kühnelt, W. Cistjakov, and U. Krewer, *J. Electrochem. Soc.*, **169**, 040550 (2022).
- H.-K. Kim, P. Barai, K. Chavan, and V. Srinivasan, *Journal of Solid State Electrochemistry*, **26**, 2059 (2022).
- M. Schleutker, J. Bahner, C.-L. Tsai, D. Stolten, and C. Korte, *Physical chemistry chemical physics : PCCP*, **19**, 26596 (2017).
- D. Brogioli, F. Langer, R. Kun, and F. La Mantia, *ACS applied materials & interfaces*, **11**, 11999 (2019).
- J. A. Isaac, L. R. Mangani, D. Devaux, and R. Bouchet, *ACS applied materials & interfaces*, **14**, 13158 (2022).
- J. Janek and W. G. Zeier, *Nat. Energy*, **1**, 1167 (2016).
- P. Minnmann, L. Quillman, S. Burkhardt, F. H. Richter, and J. Janek, *J. Electrochem. Soc.*, **168**, 040537 (2021).
- D. T. Hallinan and N. P. Balsara, *Annu. Rev. Mater. Res.*, **43**, 503 (2013).
- M. Safari and C. Delacourt, *J. Electrochem. Soc.*, **158**, A63 (2011).
- J. Lopez, A. Pei, J. Y. Oh, i. N. Wang, Y. Cui, and Z. Bao, *J. Am. Chem. Soc.*, **140**, 11735 (2018).
- S.-L. Wu, A. E. Javier, D. Devaux, N. P. Balsara, and V. Srinivasan, *J. Electrochem. Soc.*, **161**, A1836 (2014).
- A. Mistry, L. S. Grundy, D. M. Halat, J. Newman, N. P. Balsara, and V. Srinivasan, *J. Electrochem. Soc.*, **169**, 040524 (2022).
- K. M. Diederichsen, E. J. McShane, and B. D. McCloskey, *ACS Energy Lett.*, **2**, 2563 (2017).
- J. Landesfeind, J. Hattendorff, A. Ehrl, W. A. Wall, and H. A. Gasteiger, *J. Electrochem. Soc.*, **163**, A1373 (2016).
- A. Bielefeld, D. A. Weber, R. Rueß, V. Glavas, and J. Janek, *J. Electrochem. Soc.*, **169**, 020539 (2022).
- H. Wang, J. Lin, X. Zhang, L. Wang, J. Yang, E. Fan, F. Wu, R. Chen, and L. Li, *ACS Appl. Energy Mater.*, **4**, 6205 (2021).
- Y. Kwon, Y. Lee, S.-O. Kim, H.-S. Kim, K. J. Kim, D. Byun, and W. Choi, *ACS applied materials & interfaces*, **10**, 29457 (2018).
- B. Lu, Y. Song, Q. Zhang, J. Pan, Y.-T. Cheng, and J. Zhang, *Physical chemistry chemical physics : PCCP*, **18**, 4721 (2016).
- M. Wetjen, G.-T. Kim, M. Joost, G. Appetecchi, M. Winter, and S. Passerini, *Journal of Power Sources*, **246**, 846 (2014).
- A. Nyman, T. G. Zavalis, R. Elger, M. Behm, and G. Lindbergh, *J. Electrochem. Soc.*, **157**, A1236 (2010).
- L. Kraft, J. B. Hadedank, A. Frank, A. Rheinfeld, and A. Jossen, *J. Electrochem. Soc.*, **167**, 013506 (2020).
- J. Sturm, A. Rheinfeld, I. Zilberman, F. B. Spingler, S. Kosch, F. Frie, and A. Jossen, *Journal of Power Sources*, **412**, 204 (2019).
- A. Saltelli, P. Annoni, I. Azzini, F. Campolongo, M. Ratto, and S. Tarantola, *Comput. Phys. Commun.*, **181**, 259 (2010).
- A. Saltelli, K. Aleksankina, W. Becker, P. Fennell, F. Ferretti, N. Holst, S. Li, and Q. Wu, *Environmental Modelling & Software*, **114**, 29 (2019).
- I. Sobol, *Mathematics and Computers in Simulation*, **55**, 271 (2001).
- N. Lin, X. Xie, R. Schenkendorf, and U. Krewer, *J. Electrochem. Soc.*, **165**, A1169 (2018).
- S. Marelli and B. Sudret, *Vulnerability, Uncertainty, and Risk*, ed. M. Beer, S.-K. Au, and J. W. Hall (American Society of Civil Engineers, Reston, VA) p. 2554 (2014).
- C.-H. Chen, F. Brosa Planella, K. O'Regan, D. Gastol, W. D. Widanage, and E. Kendrick, *J. Electrochem. Soc.*, **167**, 080534 (2020).
- J. Landesfeind, *PhD thesis*, Technical University Munich (2018).
- H. Erabhoina and M. Thelakkat, *Sci. Rep.*, **12**, 5454 (2022).
- M. A. Roscher, J. Vetter, and D. U. Sauer, *Journal of Power Sources*, **191**, 582 (2009).
- V. Srinivasan and J. Newman, *Journal of Power Sources*, **151**, A1517 (2004).
- A. Mistry et al., *ACS Energy Lett.*, **6**, 3831 (2021).